



The competing effects of terrestrial evapotranspiration and raindrop re-evaporation on the deuterium excess of continental precipitation

Zhengyu Xia*, Matthew J. Winnick

Department of Geosciences, University of Massachusetts Amherst, Amherst, MA, USA



ARTICLE INFO

Article history:

Received 18 February 2021
 Received in revised form 18 July 2021
 Accepted 19 July 2021
 Available online 3 August 2021
 Editor: Y. Asmerom

Keywords:

precipitation
 deuterium excess
 evapotranspiration
 raindrop re-evaporation
 vapor transport model
 South America

ABSTRACT

The deuterium excess (d-excess) of precipitation, which tracks kinetic fractionations during water phase changes, has been used to trace the regions and conditions of oceanic moisture sources, in particular from polar ice-core records. Still, many observations suggest that precipitation d-excess varies significantly across terrestrial environments, both above and below the global average value 10. These variations are often interpreted to reflect either moisture recycling via terrestrial evapotranspiration or sub-cloud raindrop re-evaporation, respectively. Despite being frequently mentioned in literature, however, little work has been carried out to quantify these two competing effects on the widespread variations of d-excess. Here, we use a one-dimensional model of water vapor transport to interrogate the relative controls on d-excess of continental precipitation. We show that when the water vapor gradient is coupled with decreasing temperature, d-excess increases with net rainout and $\delta^{18}\text{O}$ depletion along the model transect, while the magnitude of increase is controlled by the water balance, evaporation/transpiration ratio, and transport type. Raindrop re-evaporation functions as an additional flux of recycled moisture and further increases the d-excess downwind. Alternatively, when the water vapor gradient is coupled with decreasing relative humidity, d-excess may decrease along the model transect wherein upwind evapotranspiration is overwhelmed by local raindrop re-evaporation effects. This local effect becomes even stronger under a regime of turbulent eddy transport with high transpiration fractions, resulting in a pronounced decrease of d-excess without notable changes in $\delta^{18}\text{O}$. Finally, we demonstrate that model processes capture the isotopic variations in precipitation across the altitudinal gradient of the Andes as well as the South American low-level jet zone. Broadly, this study presents a novel framework for understanding the dynamical controls of precipitation d-excess and for linking spatial isotopic variations with ecohydrological fluxes and processes in both modern and paleo-environments.

© 2021 Elsevier B.V. All rights reserved.

1. Introduction

The stable isotopes of hydrogen and oxygen in precipitation are useful tracers of the hydrological cycle, and their signals preserved in terrestrial archives such as ice cores, speleothems, and paleosols are commonly used for the reconstruction of past climates. The deuterium excess (d-excess) of precipitation is a second-order isotopic parameter defined as $\delta^2\text{H} - 8\delta^{18}\text{O}$ (Dansgaard, 1964), which largely reflects kinetic fractionations during water phase changes. Isotope theory suggests that the d-excess of precipitation mainly tracks kinetic fractionation processes at the site of oceanic evaporation, with a global mean value of 10‰ that characterizes the well-known Global Meteoric Water Line. As such, it is mostly interpreted as a tracer for precipitation moisture source regions and

climate conditions (Merlivat and Jouzel, 1979; Jouzel and Merlivat, 1984; Pfahl and Sodemann, 2014). In polar ice cores it has also been used to document past changes in surface ocean conditions and ocean/atmosphere circulation patterns (e.g., Vimeux et al., 1999). This classic mechanism for the d-excess variability is likely dominant for maritime, coastal, and polar areas where the hydrological cycle is highly sensitive to oceanic evaporation.

Across terrestrial environments, however, precipitation isotope data such as those collected by the Global Network of Isotopes in Precipitation (GNIP) program (IAEA/WMO, 2020) show that d-excess is highly variable regionally, ranging between 0‰ and 20‰ (Putman et al., 2019). A variety of factors can affect precipitation d-excess, but there are two major mechanisms frequently invoked in literature to explain the observed d-excess variations. First, moisture recycling that involves kinetic fractionation returns relatively high d-excess water vapor back to the atmosphere, thereby increasing d-excess in downwind atmospheric water vapor and precipitation (Gat and Matsui, 1991). Studies have found that precip-

* Corresponding author.

E-mail address: zhengyuxia@umass.edu (Z. Xia).

itation d-excess is relatively high downwind of large lakes (Gat et al., 1994) and rainforests where partial evaporation may occur from canopy storage (Gat and Matsui, 1991). Indeed, moisture recycling is ubiquitous and an essential part of the global hydrological cycle, and van der Ent et al. (2014) estimated that 36% of the global terrestrial precipitation originates from terrestrial moisture sources. Second, sub-cloud raindrop re-evaporation during rainfall events results in lower d-excess in local precipitation (Stewart, 1975; Liebming et al., 2006) and is more pronounced in warm and dry areas (Putman et al., 2019). As these two mechanisms have opposite effects, the d-excess variability across terrestrial environments reflect a balance of remote (moisture recycling) and local (raindrop re-evaporation) processes along the moisture transport pathway, that alters oceanic source values. However, there has been little effort to assess the relative importance of these two competing processes in the spatial variations in d-excess (Froehlich et al., 2008; Pang et al., 2011).

Herein, we describe a theoretical approach to characterize the competing effects of terrestrial evapotranspiration (ET) and raindrop re-evaporation on the coupled changes and spatial gradients of precipitation $\delta^{18}\text{O}$ and d-excess, as illustrated in our conceptual diagram Fig. 1. This approach builds off a previously developed one-dimensional (1-D) reactive transport model for stable isotopes in atmospheric moisture (Winnick et al., 2014) and includes new parameterizations for both fractionations in ET recycling and raindrop re-evaporation. While the most recent isotope-enabled general circulation models have been coupled to land surface models and are potential tools to investigate similar processes (e.g., Risi et al., 2016; Wong et al., 2017), our parsimonious model allows for an intuitive understanding of the complex mechanisms, effects of key model parameters, and idealized patterns of isotopic gradients. We combine new model insights from theoretical model experiments with GNIP isotope data from South America to demonstrate the power of the model as an interpretive framework for spatial isotope data.

2. Model

2.1. Reactive transport model for atmospheric moisture

Following Hendricks et al. (2000) and Winnick et al. (2014), the mass balance equation for atmospheric water vapor is:

$$\frac{dw}{dt} = \nabla(K\nabla w) - v\nabla w + ET - P, \quad (1)$$

where w is column-integrated precipitable water, K is the coefficient of turbulent eddy diffusion, v is advection velocity, ET is evapotranspiration flux, and P is precipitation. Assuming a steady-state condition within a 1-D domain, Eq. (1) is non-dimensionalized and expressed in delta notation of isotope ratios as:

$$\frac{d\delta_a}{dx'} + (\delta_p - \delta_a) - N_d(\delta_{ET} - \delta_p) = 0 \quad (2)$$

for transport by advection only and

$$\frac{d^2\delta_a}{dx'^2} - 2\frac{d\delta_a}{dx'} - (\delta_p - \delta_a) + N_d(\delta_{ET} - \delta_p) = 0 \quad (3)$$

for transport by turbulent eddy diffusion only (Hendricks et al., 2000). Here, δ_a , δ_p , δ_{ET} are the isotopic composition of atmospheric water vapor, precipitation, and ET, respectively, x' is the dimensionless distance as $x' = x/\ell$ with the length scale of atmospheric water vapor loss $\ell = -w(dx/dw)$, and N_d is the Damköhler number that can be expressed as $N_d = ET/(P - ET)$ to relate the ET flux

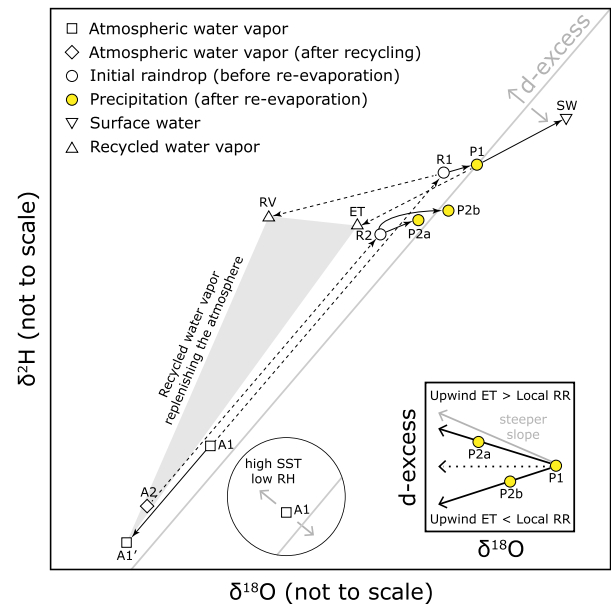


Fig. 1. The conceptual diagram showing the evolution of $\delta^2\text{H}$ and $\delta^{18}\text{O}$ in the terrestrial hydrological cycle. Dashed arrows in the main plot indicate isotopic fractionations during phase changes and solid arrows indicate changes in the remaining composition. The isotopic composition of atmospheric water vapor (A1) derived from oceanic evaporation is sensitive to the moisture source condition, and its d-excess increases under lower RH and/or higher sea surface temperature (SST). That atmospheric water vapor undergoes rainout as it is transported inland. The raindrop (R1) formed in isotopic equilibrium with atmospheric water vapor experiences sub-cloud raindrop re-evaporation (RR). The final raindrop that reaches the ground is precipitation (P1), the amount and isotopic composition of which reflect ground-based measurements. The precipitation feeds the surface water (SW) pool, some of which is recycled back to the atmosphere via evapotranspiration (ET). The recycled water vapor by ET and RR (denoted as RV, i.e., the raindrop-derived vapor) replenishes the isotopically depleted atmospheric water vapor (A1') transported further inland, increasing its d-excess (A2). As such, the precipitation in downwind areas should track the higher d-excess signal (R2 and P2a). However, if the local RR effect becomes stronger, it can overprint the upwind ET effect and cause a lower d-excess (P2b) compared to P1. The inset diagram shows the consequence of these two competing effects in terms of the evolution of $\delta^{18}\text{O}$ and d-excess (solid arrows) in response to transport and rainout of water vapor. The traditional interpretation that d-excess serves as a quasi-conservative tracer for oceanic conditions (shown in dotted arrows) thus does not consider the dynamical processes across terrestrial environments, which may be captured by analyzing the relationship between d-excess and $\delta^{18}\text{O}$, such as their slope.

to the transport flux (see Winnick et al., 2014). Assuming an initial condition $w = w_0$ when $x' = 0$, the term ℓ can be eliminated and we derive a simple expression for x' as $\exp(-x') = w/w_0$. The analytical solutions to Eqs. (2) and (3) are:

$$\delta_a = (\delta_a^0 - \delta_a^\infty) \left(\frac{w}{w_0}\right)^{\alpha + \alpha N_d - 1} + \delta_a^\infty \quad (4)$$

and

$$\delta_a = (\delta_a^0 - \delta_a^\infty) \left(\frac{w}{w_0}\right)^{\sqrt{\alpha + \alpha N_d} - 1} + \delta_a^\infty, \quad (5)$$

respectively, where

$$\delta_a^\infty = \frac{N_d \delta_{ET} - (1 + N_d)(\alpha - 1) 10^3}{\alpha + \alpha N_d - 1} \quad (6)$$

and δ_a^0 and δ_a^∞ are the initial ($w = w_0$) and ultimate ($w \rightarrow 0$) isotopic composition of atmospheric water vapor, respectively. Here, α is the apparent fractionation factor between water vapor and precipitation combining the equilibrium fractionation from vapor to liquid (α_{l-v}) and the fractionation associated with raindrop re-evaporation (α_{RR} ; see Section 2.3) as $\alpha = \alpha_{l-v} \alpha_{RR}$. As the function

for δ_a is iterated throughout the model transect, the corresponding δ_p is calculated as:

$$\delta_p = (\delta_a + 1000)\alpha - 1000. \quad (7)$$

Note that α should be modified for freezing temperatures to represent the ice-vapor fractionation, which is not within the scope of our analysis.

The vapor transport framework presented above has limitations due to its 1-D configuration. In particular, it does not simulate convective processes and is unable to account for vertical motion and mixing that are important in the tropics. The model is aimed to represent the mass-balance relation of atmospheric water vapor and the evolution of its isotopes over spatial scales on timescales much longer than individual convective storm events (Winnick et al., 2014; Kukla et al., 2019).

2.2. δ_{ET} parameterization

To capture the feedback of terrestrial ET on the spatial evolution of δ_a and δ_p , it is imperative to have a simple parameterization for δ_{ET} . We assume that transpiration involves no fractionation while the fractionation from evaporation combines equilibrium and kinetic fractionations based on the Craig and Gordon (1965) model (Williams et al., 2004). With the local precipitation (R_p) as the source water, the instantaneous isotope ratio (R) of ET (R_{ET}^0) is:

$$R_{ET}^0 = \left(\frac{E}{ET}\right) \left(k \frac{\alpha_{v-l} R_p - h R_v}{1-h}\right) + \left(\frac{T}{ET}\right) R_p, \quad (8)$$

where $\frac{E}{ET}$ and $\frac{T}{ET}$ are the evaporated and transpired fraction of ET, respectively, k is the kinetic fractionation factor of evaporation, α_{v-l} is the equilibrium fractionation factor from liquid to vapor ($1/\alpha_{l-v}$), R_v is the isotope ratio of near-surface vapor, and h is relative humidity (RH). Rearranging Eq. (8) with the implementation of closure assumption as $R_v = R_{ET}^0$ (Aemisegger et al., 2014) gives:

$$R_{ET}^0 = \left(\frac{E}{ET}\right) \left[k \frac{\alpha_{v-l} R_p}{(1-h) \left(1 + k \frac{E}{ET} \frac{h}{1-h}\right)} \right] + \left(\frac{T}{ET}\right) \left(\frac{R_p}{1 + k \frac{E}{ET} \frac{h}{1-h}} \right). \quad (9)$$

To incorporate the water balance effect following Caves et al. (2015), the isotopic composition of integrated ET flux is modeled based on the Rayleigh-type progressive removal of liquid water as:

$$\delta_{ET} = \left(\frac{E}{ET}\right) \frac{\int_1^f [\alpha_{ET} (\delta_p + 1000)] f^{\alpha_{ET}-1} - 1000] df}{f-1} + \left(\frac{T}{ET}\right) \delta_p, \quad (10)$$

where $\alpha_{ET} = R_{ET}^0/R_p$, which is the apparent fractionation factor of evaporation that is affected by the concurrent transpiration, and $f = (P - ET)/P = 1/(1 + N_d)$, which is the fraction of residual liquid water remaining in the terrestrial water storage.

Equation (10) conveniently predicts δ_{ET} with just a few parameters (Fig. 2), but it hinges on the closure assumption for total ET flux and the Rayleigh-type fractionation, both of which are invalid over short timescales (e.g., Lee et al., 2007). In addition, it treats evaporation as a bulk flux and does not distinguish the physical mechanism of evaporation from different water pools such as soils, lakes, and forest canopy. Therefore, its form is based on theoretical considerations. It should be noted that in this parameterization, when T/ET is higher, δ_{ET} becomes very close to δ_p (including the

d-excess), and when RH is close to 100%, δ_{ET} does not equal to δ_p (but with similar d-excess) (Figs. 2). These two features differ from that predicted from the steady-state evaporation model by Gat and Matsui (1991), despite their similarity in the overall relationship between δ_{ET} and those parameters (Fig. S1).

2.3. Raindrop re-evaporation model

We use heat and mass transfer equations to model the raindrop re-evaporation effect, following the approach by Graf et al. (2019). A detailed description of model functions and parameters are presented in the Supplemental Materials and Table S1 and outlined briefly here. First, given a local surface temperature and RH, the lifting condensation level (LCL) is derived from the expression by Roms (2017), along with vertical profiles of temperature, pressure, RH below the LCL. Next, a particular size of raindrop is released at the LCL height, with its initial isotopic composition ($R_{initial}$) in equilibrium with that of atmospheric water vapor. It falls with a speed dependent on raindrop size (Fig. S2) through the sub-cloud background water vapor that has the same isotopic composition as the atmospheric water vapor. Then, the change in raindrop mass (dm) is calculated for each time step of $dt = 0.1$ s until it reaches the ground as:

$$\frac{dm}{dt} = \frac{2\pi df_v D}{R_w} \left(h \frac{e_{sat, T_\infty}}{T_\infty} - \frac{e_{sat, T_d}}{T_d} \right), \quad (11)$$

where d is raindrop diameter, f_v is the mass ventilation coefficient of water vapor, D and R_w are the diffusivity and specific gas constant of water vapor, respectively, h is the ambient RH, and e_{sat, T_∞} and e_{sat, T_d} are the saturation vapor pressure for the ambient air (at ambient temperature T_∞) and for the thin boundary layer in contact with the raindrop (at raindrop temperature T_d), respectively. Equation (11) can be written similarly for individual heavy isotope species (^{18}O and ^2H) as:

$$\frac{dm'}{dt} = \frac{2\pi df_v D}{R_w} \left(\frac{f'_v D'}{f_v D} \right)^n \left(h \frac{e'_{sat, T_\infty}}{T_\infty} - \frac{e'_{sat, T_d}}{T_d} \right), \quad (12)$$

where the prime symbol refers to quantities for heavy isotope species and the exponent n is 0.58 determined by Stewart (1975) to account for partial diffusion.

The raindrop temperature, T_d , is required for Eqs. (11) and (12). Assuming $T_d = T_\infty$ when the initial raindrop is formed, the change in T_d for each time step while falling must balance the latent heat loss due to evaporation and the sensible heat flux from warmer ambient air and is calculated as:

$$\frac{dT_d}{dt} = \frac{12}{d^2 \rho_w c_w} \left[\frac{L_e f_v D}{R_w} \left(h \frac{e_{sat, T_\infty}}{T_\infty} - \frac{e_{sat, T_d}}{T_d} \right) - f_h k_a (T_d - T_\infty) \right], \quad (13)$$

where ρ_w and c_w are the density and specific heat of liquid water, respectively, L_e is the latent heat of evaporation, f_h and k_a are the heat ventilation coefficient and thermal conductivity of air, respectively.

By calculating Eqs. (11)–(13) over the falling time of a raindrop, we finally derive the percentage of mass loss from the initial raindrop, final raindrop diameter, and final isotopic ratios (R_{final}). The fractionation factor associated with raindrop re-evaporation is calculated as $\alpha_{RR} = R_{final}/R_{initial}$. Fig. 3 shows that surface temperature, surface RH, and initial raindrop size together determine the magnitude of raindrop re-evaporation and its isotopic expressions. In fact, surface RH plays a more prominent role than surface temperature because it is more important to determine the LCL height and falling duration. We note that iteration breaks down when the

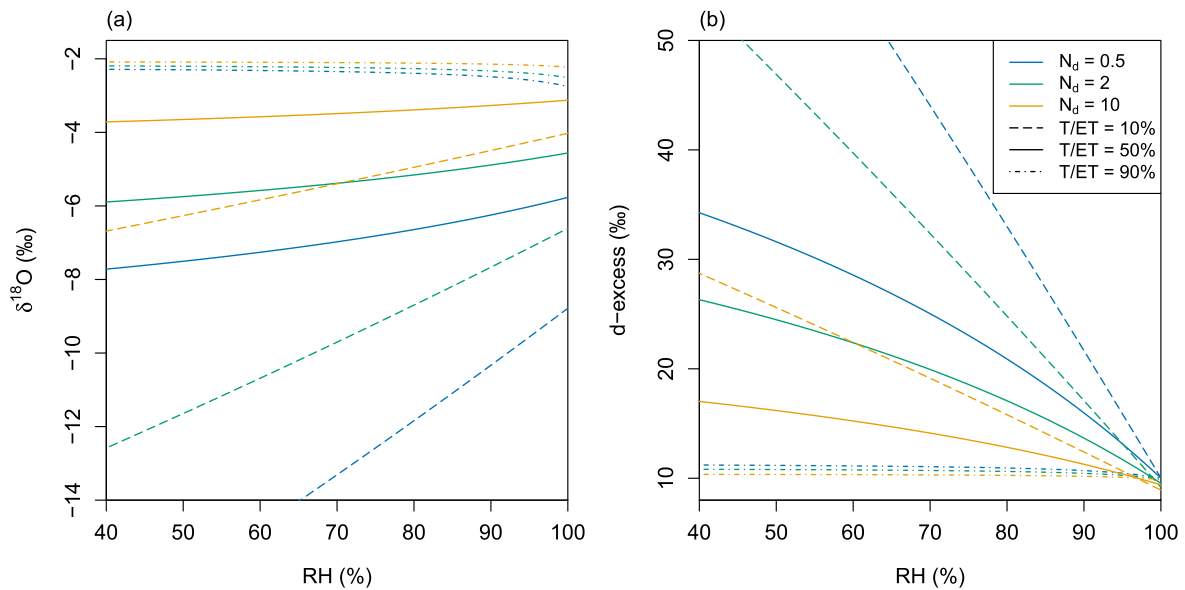


Fig. 2. The sensitivity of (a) $\delta^{18}\text{O}$ and (b) d-excess of ET to RH, N_d , and T/ET in our parameterization. The surface temperature is assumed to be 25°C, and the input precipitation $\delta^{18}\text{O}$ and d-excess are -2‰ and 10‰, respectively. A description of fractionation factors can be found in Section 4.

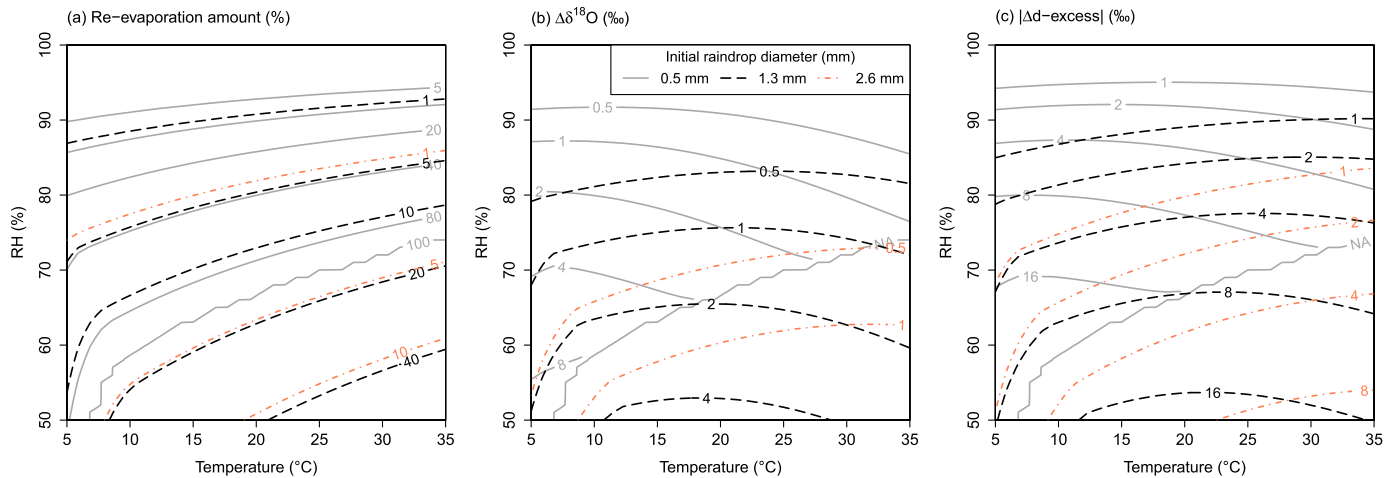


Fig. 3. The isotopic effects of raindrop re-evaporation. (a) The percentage of re-evaporative loss of initial raindrop mass, (b) relative increase of raindrop $\delta^{18}\text{O}$, and (c) relative decrease of d-excess are shown as contour lines given the conditions of surface temperature, RH, and initial raindrop size. The initial raindrop $\delta^{18}\text{O}$ and d-excess are -2‰ and 10‰, respectively. Three initial raindrop diameters (0.5 mm, 1.3 mm, and 2.6 mm) are chosen to represent the typical raindrop size for drizzle rains (less than 1 mm/hr), normal rains (3 mm/hr), and heavy rains (higher than 30 mm/hr) (Fig. S4; Best, 1950). Note that when the initial raindrop diameter is very small (0.5 mm), the raindrop will be evaporated completely on the way before reaching the ground under warm and dry conditions ("NA" in lower right corner).

residual mass of raindrop is too small, at which point the raindrop is assumed completely evaporated before reaching the ground.

One important assumption to model raindrop re-evaporation here is that the background water vapor is in isotopic equilibrium with the raindrop when it starts to fall into the sub-cloud layer. A different isotopic composition for the background water vapor, namely a different $e'_{\text{sat}, T_{\infty}}$ in Eq. (12), can affect the exchange of isotope species for raindrops (Fig. S3), a process analogous to isotopic equilibration in an environment of $\text{RH} = 100\%$ (Lee and Fung, 2008). The role of this isotopic exchange may be important in convective processes where higher-level water vapor is injected into the sub-cloud layer by unsaturated downdrafts (Risi et al., 2008). Further, if the hydrometeor is formed at a higher, freezing cloud level and experiences other isotopic modifications while falling within the cloud, its isotopic composition may deviate from the isotopic equilibrium with the sub-cloud vapor, leading to additional isotopic exchange (Graf et al., 2019). Although the isotopic composition of the sub-cloud layer can dictate the isotopic compo-

sition of precipitation during and between rainfall events, this level of complexity is not considered. The primary interest to couple the raindrop re-evaporation model with the vapor transport model is to capture the steady-state isotopic effects in the net transfer of water molecules represented by re-evaporation flux on longer timescales.

3. Data

3.1. Isotope data

For model-data comparisons, GNIP monthly precipitation isotope data from South America are compiled (IAEA/WMO, 2020). Amount-weighted monthly mean and standard deviation of precipitation $\delta^{18}\text{O}$ and d-excess are calculated for each season: December–February (DJF), March–May (MAM), June–August (JJA), and September–November (SON). For data quality control, we only include the monthly measurement if the $\delta^{18}\text{O}$ value is lower than

2‰ and d-excess value is between -10‰ and 30‰ . We select only stations with at least three d-excess data for a given season. We use the Hybrid Single-Particle Lagrangian Integrated Trajectory model (HYSPLIT) to constrain the seasonal moisture transport pathway for these stations (Stein et al., 2015; Warner, 2018). Daily back-trajectories are computed for each station using the one-degree Global Data Assimilation System reanalysis from 2005–2019. The initial back-trajectory height is arbitrarily set at 1500 m above ground level and 2000 m if the altitude is >1500 m above sea level to further reduce the effect of topography barriers. Different initial back-trajectory heights usually produce qualitatively similar results (Fiorella et al., 2015). Contour maps of precipitation amount-weighted trajectory frequency are used to assess whether a chain of stations suffice for an idealized 1-D transect for a given season. Supplementary Materials contain the summary of isotope dataset and HYSPLIT model results.

3.2. Model parameters

Reanalysis products for model parameters are used in our model-data comparison, including average ERA5 2-m air temperature (T2m), 2-m RH (calculated with 2-m dew temperature), and total column water vapor (TCWV) from 1981–2010. For N_d calculations, we use average 1981–2010 ET flux from the Global Land Evaporation Amsterdam Model (GLEAM) v3.2a (Martens et al., 2017) and precipitation flux from the Multi-Source Weighted-Ensemble Precipitation dataset v2.2 (Beck et al., 2019). Previous applications of the model calculated N_d using reanalysis-based runoff data so that $N_d > 0$ (Winnick et al., 2014). In this study we use the GLEAM ET product and allow $P < ET$ on seasonal timescales. However, the model-data comparison is only carried out for regions where $P > ET$ ($N_d > 0$), because negative N_d values are inconsistent with our definition of length scale. This situation will be addressed in the future.

For raindrop diameter, we explore the Tropical Rainfall Measuring Mission (TRMM) 3B42 3-hr rainfall data (Huffman et al., 2007) as the statistical distribution of raindrop size can be linked to rainfall rate as (Fig. S4; after Best, 1950):

$$f(d) = \exp\left[-\left(\frac{d}{1.3I^{0.232}}\right)^{2.25}\right] \frac{2.25d^{1.25}}{(1.3I^{0.232})^{2.25}}, \quad (14)$$

where $f(d)$ is the mass fraction of a particular raindrop diameter d (mm) at a rainfall rate of I (mm/hr). The expression by Best (1950) is based on ground measurements of raindrop size and the TRMM-based rainfall is also calibrated by rain gauge data, whereas the raindrop re-evaporation model requires the input of initial raindrop diameter at the LCL. For this reason, we first calculate the total final raindrop size distribution for a given TRMM grid by summing the amount-weighted raindrop size distributions of all individual rainfall events during the TRMM period (1998–2019). Next, we inversely infer the initial raindrop size distribution from the TRMM-based final raindrop size distribution using the raindrop re-evaporation model with ERA5 T2m and RH data. Then, we determine the mass fraction-weighted α_{RR} from the initial raindrop size distribution, and finally find the single, representative value of initial raindrop diameter that will produce the same α_{RR} (Fig. S5). This representative initial raindrop diameter is used to calculate α_{RR} when running the vapor transport model for model-data comparisons.

4. Isotopic variations from idealized model experiments

To investigate the theoretical behavior of spatial isotopic variations from the model, we consider two different scenarios of terrestrial water vapor transport and rainout (Fig. 4). In Scenario

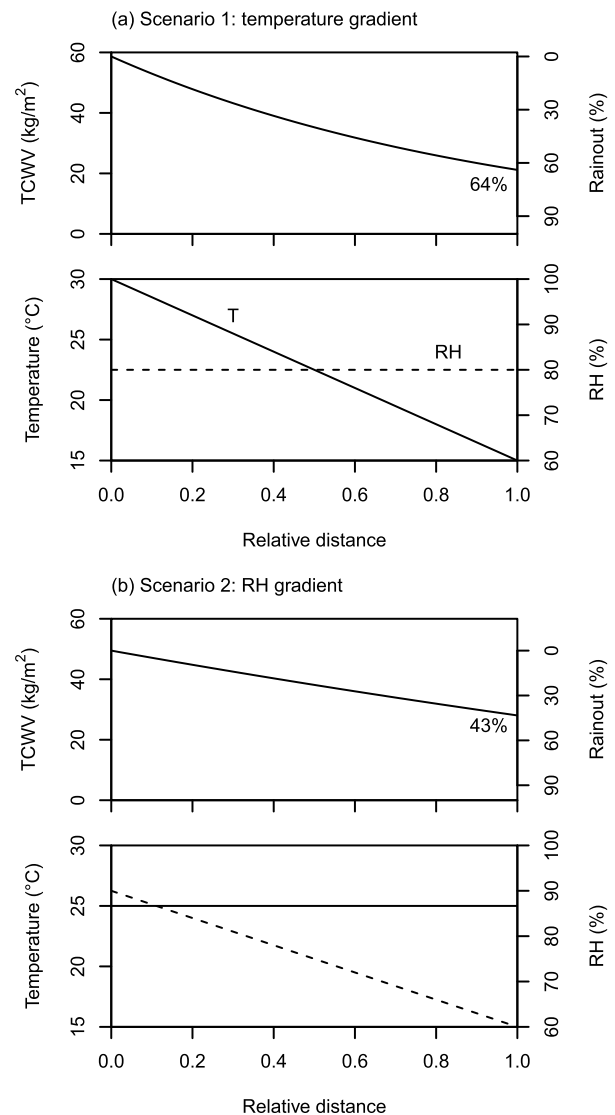


Fig. 4. The scenario of water vapor gradient with (a) temperature gradient and (b) RH gradient for idealized model experiments.

1, surface temperature decreases from 30 °C to 15 °C with a constant surface RH of 80%, representing the horizontal vapor transport over certain altitudinal gradients or large-scale poleward vapor transport. In Scenario 2, surface RH decreases from 90% to 60% with a constant surface temperature of 25 °C , representing the continental-scale vapor transport towards the drier interior. In the iteration of Eqs. (4)–(7) for such idealized model experiments, we couple the water vapor content gradient (the net rainout) with the temperature and RH gradient using the Smith (1966) equation as:

$$w = 10 \exp[0.1133 - \ln(\lambda + 1) + 0.0393(1.8T_{LCL} - 459.67)], \quad (15)$$

where w also represents the TCWV (kg/m^2), the fitting number λ is around 3 for low latitudes, and T_{LCL} is the LCL temperature (in Kelvin) that decreases with either decreasing surface temperature or decreasing surface RH. We note that previous applications of the model have kept the surface temperature and RH constant along the transport pathway but force the model with a particular degree of rainout (Winnick et al., 2014; Caves et al., 2015). The current setup recognizes the reality that moisture transport and

progressive rainout across terrestrial environments are established with climate gradients.

For both scenarios, we run the model for two transport types, with T/ET values from 10% to 90% and several N_d values including 0 (no ET) and from 0.5 ($ET = 0.33P$) to 20 ($ET = 0.95P$) that characterize the shift from modern wet areas with a large moisture surplus to dry areas with an efficient moisture recycling. The initial precipitation $\delta^{18}O$ and d-excess are -2‰ and 10‰ , respectively. The equilibrium fractionation factors α_{l-v} in Eqs. (4)–(7) and α_{v-l} in Eqs. (8) and (9) are calculated based on the LCL and surface temperature, respectively, using the equations by Majoube (1971). The kinetic fractionation factor of evaporation k in Eqs. (8) and (9) is $(D'/D)^q$ where D'/D is the ratio of diffusivity of water vapor between heavy and light isotope species. The exponent q depends on the boundary-layer aerodynamics above the evaporation front. It ranges from 0.5 to 1 for soil environments from wet to dry conditions (Mathieu and Bariac, 1996) and is further lower for large lakes (Gat et al., 1994). For simplicity, we take $q = 0.8$ in this study, while it should be noted that a smaller q value weakens the kinetic effect on d-excess. The equations for α_{l-v} and values for D'/D and k can be found in Table S1. We assume a relatively small initial raindrop diameter 1 mm characteristic of a rainfall rate of 1 mm/hr (Fig. S4) to enlarge the raindrop re-evaporation effect, and for comparison we additionally run the model with raindrop re-evaporation disabled ($\alpha_{RR} = 1$).

Fig. 5 summarizes the results of idealized model experiments. As the previous study by Winnick et al. (2014) has investigated the sensitivity of $\delta^{18}O$ gradient to different model parameters, we focus on the relationship or the slope between d-excess and $\delta^{18}O$, that is, the gradient of d-excess referenced to $\delta^{18}O$, a form that we want to explore further as shown in our conceptual diagram (Fig. 1).

Under the temperature gradient scenario, precipitation d-excess increases linearly as $\delta^{18}O$ decreases following rainout for advection-only transport, and d-excess/ $\delta^{18}O$ slopes become steeper under both higher N_d and lower T/ET conditions (Fig. 5a). This suggests that given a rainout profile, more efficient moisture recycling and higher evaporation fractions of ET lead to higher d-excess for the same depletion of $\delta^{18}O$. For eddy-only transport, the final $\delta^{18}O$ at the end of transect is much less depleted, and model curves show steeper d-excess/ $\delta^{18}O$ slopes (Fig. 5b). In contrast to advection-only transport, however, lower T/ET values can cause shallower rather than steeper d-excess/ $\delta^{18}O$ slopes (e.g., $N_d = 10$ orange curves in Fig. 5b). The steeper d-excess/ $\delta^{18}O$ model curves for eddy-only transport primarily result from the fact that d-excess is relatively insensitive to eddy mixing that would flatten the $\delta^{18}O$ or δ^2H gradient versus distance through the square root term for the fractionation factor in Eq. (5) (Winnick et al., 2014), thus the same d-excess change is reflected across a smaller $\delta^{18}O$ change. When T/ET values are lower, the higher d-excess in ET flux is more important than its lower $\delta^{18}O$ in moisture recycling for advection-only transport, thus d-excess/ $\delta^{18}O$ slopes become steeper; however, the opposite can be true for eddy-only transport and results in shallower slopes.

Furthermore, if the raindrop re-evaporation effect is disabled, the results shown in inset plots of Figs. 5a and b suggest that the raindrop re-evaporation itself has slightly steepened the model curves and in a larger degree with a lower N_d value. As the local effect of raindrop re-evaporation on precipitation d-excess is insensitive to the decreasing temperature across the model transect (Fig. 3c), the further steepened model curves reflect the raindrop recycling, similar to the ET recycling (Fig. 1). The same process has been referred to as remoistening that is considered as a potential mechanism for the higher precipitation d-excess in the inland wet tropics (Noone, 2012; Putman et al., 2019). Our model provides a more comprehensive framework to quantify the relative role of

raindrop recycling, which as an invisible flux of moisture recycling has no impact on surface hydrology but affects the isotopic gradients of water vapor and precipitation (Li and Garzzone, 2017).

Under the RH gradient scenario, precipitation d-excess increases as $\delta^{18}O$ decreases only under high N_d and low T/ET conditions for advection-only transport, when ET recycling is the dominant process affecting d-excess variations across the model transect (Fig. 5c). Additionally, these two conditions result in an increased depletion of $\delta^{18}O$ plotted outside the range of x -axis. As N_d is unrelated to the net rainout in these formulations, a greater amount of ET recycling (higher N_d) also requires a greater amount of precipitation to maintain the same degree of net rainout. The mass balance effect from higher N_d strengthens the depletion of $\delta^{18}O$ and even more with lower T/ET values (Winnick et al., 2014). By contrast, under low N_d and high T/ET conditions, the depletion of $\delta^{18}O$ is reduced and d-excess decreases along the transport pathway (Fig. 5c). These different trajectories of d-excess reflect the competing effects between upwind ET and local raindrop re-evaporation. While the decreasing RH along the model transect progressively increases the d-excess of ET flux (Fig. 2b), this recycling effect is relatively weak. Instead, local raindrop re-evaporation, which becomes increasingly important at lower RH (Fig. 3c), overprints upwind ET signals and leads to progressive decreases in d-excess. The role of raindrop re-evaporation is even more pronounced for eddy-only transport, leading to large d-excess decreases with minimal changes in $\delta^{18}O$, in particular under high T/ET conditions (Fig. 5d).

We demonstrate that raindrop re-evaporation is an important mechanism to locally lower the precipitation d-excess across terrestrial environments, compared to the case with disabled raindrop re-evaporation (Figs. 5c and d). This mechanism has been invoked to explain observations of locally low d-excess continental precipitation in literature (e.g., Froehlich et al., 2008; Pang et al., 2011; Rohrmann et al., 2014), but our model analysis reveals the conditions under which this local effect can overprint upwind moisture recycling. The pattern of decreasing d-excess in response to net rainout requires a strong RH gradient, low N_d , and high T/ET , and is enhanced by turbulent eddy transport.

The above discussion presents a theoretical framework for coupled precipitation $\delta^{18}O$ and d-excess variations over continents. In Fig. 6, we specifically show the difference in slope values of those model curves, in addition to the reference slope curves shown in Fig. 5. Different temperature/RH gradients and different choices of the aerodynamic exponent, initial raindrop diameter, or initial isotopic composition do not change the overall pattern of the results. In summary, there is no single, but rather several factors that together govern the exact d-excess/ $\delta^{18}O$ slope; thus, any mechanistic interpretation of continental precipitation d-excess data should be made in the context of regional hydroclimate and transport mechanisms in addition to moisture source conditions.

5. Model-data comparison for South America

To test the model performance on real-world observations in South America, we specifically focus on altitudinal transects from South American lowlands westward over the high Andes (temperature gradient scenario) and the South American low-level jet (LLJ) zone transect east of the Andes (RH gradient scenario) where there are steep water vapor gradients (Fig. 7b). We restrict the analysis of these transects in selected seasons when there is an overall $N_d > 0$ environment (Fig. 7a) and the back-trajectory data indicate that GNIP stations are along the same moisture transport pathway (Supplementary Materials) to meet the assumption of the model framework. The vapor transport model is forced by reanalysis-based parameters across those GNIP station transects, except the T/ET , which we prescribe as 50%, 70, or 90%, covering the range

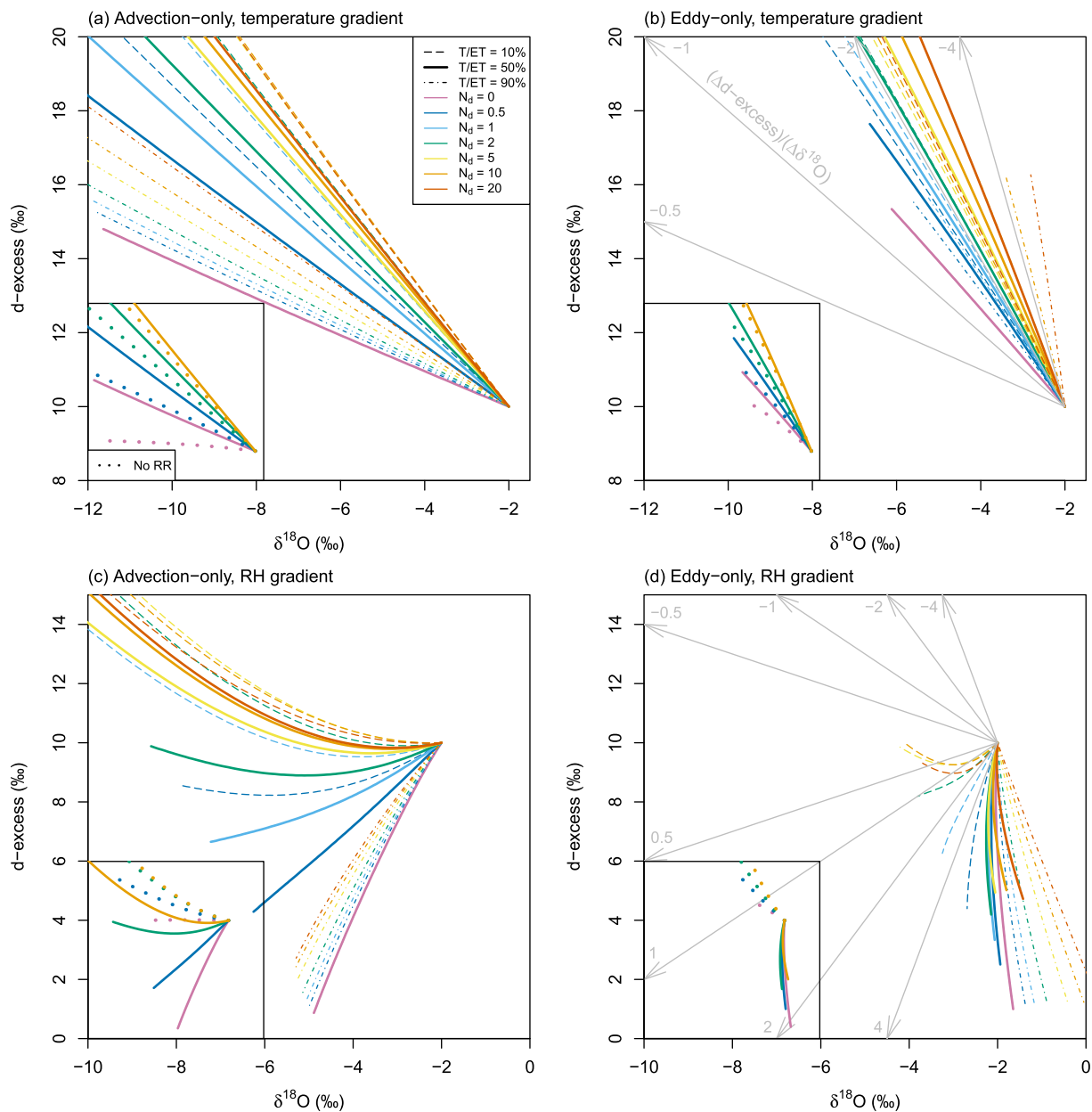


Fig. 5. The results of model experiments showing the coupled changes in precipitation $\delta^{18}\text{O}$ and d-excess under the (a, b) temperature gradient and (c, d) RH gradient, and for (a, c) advection-only and (b, d) eddy-only transports. Note that some model curves overlay others. Inset plots compare the model curves with and without the raindrop re-evaporation (RR) effect when T/ET is 50%. These inset plots have the same axis range as their respective main plots but have a reduced plot size. The reference slopes are shown in gray lines in (b) and (d) for comparison. (For interpretation of the colors in the figure(s), the reader is referred to the web version of this article.)

of literature values (Jasechko et al., 2013; Wei et al., 2017). We find that the large effective rainout for those transects allows for a more explicit analysis of the relationship between d-excess and $\delta^{18}\text{O}$ that is less prone to data errors and potential vapor mixing from outside the domain. While we acknowledge potential biases in the isotopic composition of precipitation from a few GNIP stations to the inter-annual variability of the El Niño/Southern Oscillation and land-use changes (Vuille et al., 2003; McGuffie and Henderson-Sellers, 2004), we assume that the general pattern between d-excess and $\delta^{18}\text{O}$ across multiple stations is robust for comparison with model results.

Using stable isotope data to characterize the hydrological cycle across the vast Amazon basin, in particular the partitioning of ET, has drawn wide interest (Salati et al., 1979; Gat and Matsui, 1991; Moreira et al., 1997; McGuffie and Henderson-Sellers, 2004). However, due to the limitation of the model framework, we have to

exclude areas like the Amazon basin where the water vapor gradient is small or even positive; that is, the water vapor content increases versus transport distance following trade wind easterlies, or N_d is calculated as negative values ($P < ET$), such as during JJA (Figs. 7a and b). These conditions indicate a pronounced role of terrestrial moisture sources on seasonal timescales (Gimeno et al., 2010) when ET during the dry season is partially supplied by the residual moisture from the previous wet season (Guan et al., 2015). Such dynamics require a more complex parameterization of δ_{ET} and other modifications on the vapor transport model, which will be investigated in future work.

5.1. The Andes

For the Andean altitudinal transects, GNIP data show clear trends in increasing d-excess and decreasing $\delta^{18}\text{O}$ as altitude in-

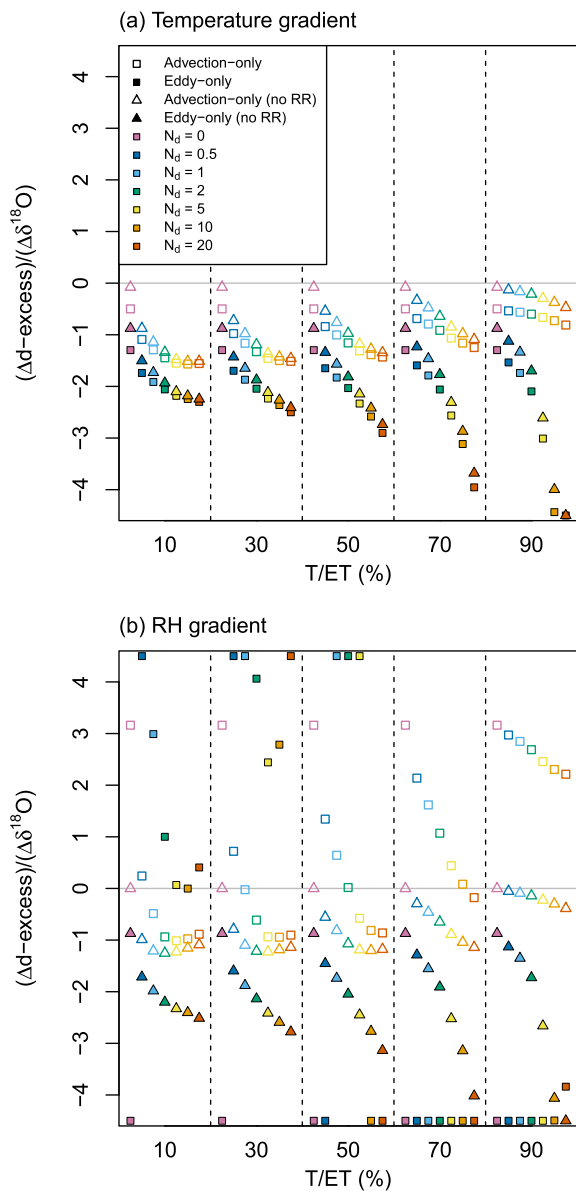


Fig. 6. The slopes between the change of d-excess and $\delta^{18}\text{O}$ under the (a) temperature gradient and (b) RH gradient as in Fig. 5. The slope value is determined for each model run once the absolute change in d-excess or $\delta^{18}\text{O}$ is more than 10‰, or at the end of transect. Some slope values are plotted at the top or bottom of plots if they are >4.5 or <-4.5 .

creases, although the d-excess/ $\delta^{18}\text{O}$ slopes vary (Figs. 8a–d). During DJF and MAM, the southern central (SC) Andes (triangles in Fig. 8a) and northern (N) Andes (Fig. 8c) transects display steeper and shallower d-excess/ $\delta^{18}\text{O}$ slopes, respectively, than the northern central (NC) Andes transect (inverted triangles in Figs. 8a and b). Also, the NC Andes transect has a steeper slope of d-excess increase during SON than other seasons (Fig. 8d).

Reanalysis data show that the temperature lapse rate dominates the water vapor gradient across the upslope section of altitudinal transects, but RH decreases sharply at the plateau or intramontane section at the end of transect, except for the N Andes (Fig. S5). The model results for the upslope section shown in main plots of Figs. 8a–d reasonably follow trends of data and capture regional differences in the d-excess/ $\delta^{18}\text{O}$ slope. The different slopes of model curves mainly reflect the variable N_d , which is as low as <1 for N Andes during MAM and as high as >10 for NC Andes during SON (Figs. 7a and S5).

While the upslope model results capture general trends of data, a more detailed model-data comparison is not straightforward for several reasons. First, an accurate initial isotopic composition as the “anchor point” for model curves is crucial but not strictly constrained. We slightly adjust the initial d-excess value from that recorded by nearby Amazon or Gran Chaco lowland stations (Fig. 8e) for a better fit with the overall trend of data. Second, the transport type itself affects the slope of model curves. The advection-only transport results in the $\delta^{18}\text{O}$ decrease and d-excess increase with shallower slopes, whereas the eddy-only transport results in smaller shifts of $\delta^{18}\text{O}$ and d-excess with steeper slopes. The actual pattern in both the amplitude and slope of coupled $\delta^{18}\text{O}$ and d-excess variations is enclosed between these two end-members and is likely closer to advection-only transport based on the mapped high Péclet number (advection/diffusion ratio, Winnick et al., 2014). Third, a number of GNIP stations are located within the end-section with decreasing RH, including stations 8, 9, 11, 12, and 19 shown in Fig. 8e. These data points marked by asterisks may obscure the overall relationship between d-excess and $\delta^{18}\text{O}$ across the transect and indeed are plotted below the expected trend from the rest of data and the model curves of the upslope section, suggesting strong local effects of raindrop re-evaporation. The exception is station 11 (El Alto), which is on the flat Bolivian Altiplano, only ~ 5 km west of but has an elevation ~ 450 m higher than station 12 (La Paz) located in a local canyon. The large d-excess offset between these two nearby stations may suggest that there is a local-scale heterogeneity in climate and precipitation processes. The eddy-only model curves for the section of decreasing RH are shown in inset plots to demonstrate that the raindrop re-evaporation theoretically could cause large local decreases of d-excess (Figs. 8a, b, and d), although the exact degree may be less pronounced if the transport is more dominated by advection as shown in idealized model experiments (Figs. 5c and d). With these uncertainties in mind, we still note that, for NC Andes and during DJF and SON, model curves of 50% or 70% T/ET have a better fit with data than that of 90% T/ET, which apparently underestimate the amplitude of d-excess shift regardless of transport types (Figs. 8a and d).

5.2. The South American low-level jet zone

For the LLJ transect with southward moisture transport over a 2000-km distance, GNIP data show much smaller ranges of $\delta^{18}\text{O}$ variability compared to the Andean altitudinal transects (Figs. 9a and d). During DJF, d-excess first increases from 10% to $>15\%$ without a notable change in $\delta^{18}\text{O}$, followed by a dramatic shift of decreasing d-excess to $<7\%$ and slightly increasing $\delta^{18}\text{O}$ (Figs. 9a and b), composing a “loop pattern” (pink arrow in Fig. 9a). During MAM, d-excess increases with slightly decreasing $\delta^{18}\text{O}$ for the entire transect (Figs. 9d and e), unlike during DJF.

The vapor transport model broadly captures these two distinct patterns of $\delta^{18}\text{O}$ and d-excess changes. Reanalysis data show that there is a small temperature gradient (less than 6°C) but large RH gradient (more than 30%) across the LLJ transect during DJF (Figs. 7c and d, and 9c). As a result, the “loop pattern” in the d-excess- $\delta^{18}\text{O}$ plot reflects the transition between the condition in which the raindrop re-evaporation effect does not and does out-compete the ET effect under the decreasing RH. To better demonstrate this transition, we split the transect into two separate model domains; the second domain covers where RH decreases from 65% to 48% (Fig. 9c) and model is reset using the isotope data from the station 26 as the estimate for the initial isotopic composition (Figs. 9a and b). For the first domain, model results are shown in the main plot of Fig. 9a and document the trend towards higher d-excess despite the divergence in model curves of different transport types. Again, we expect that the actual pattern in both am-

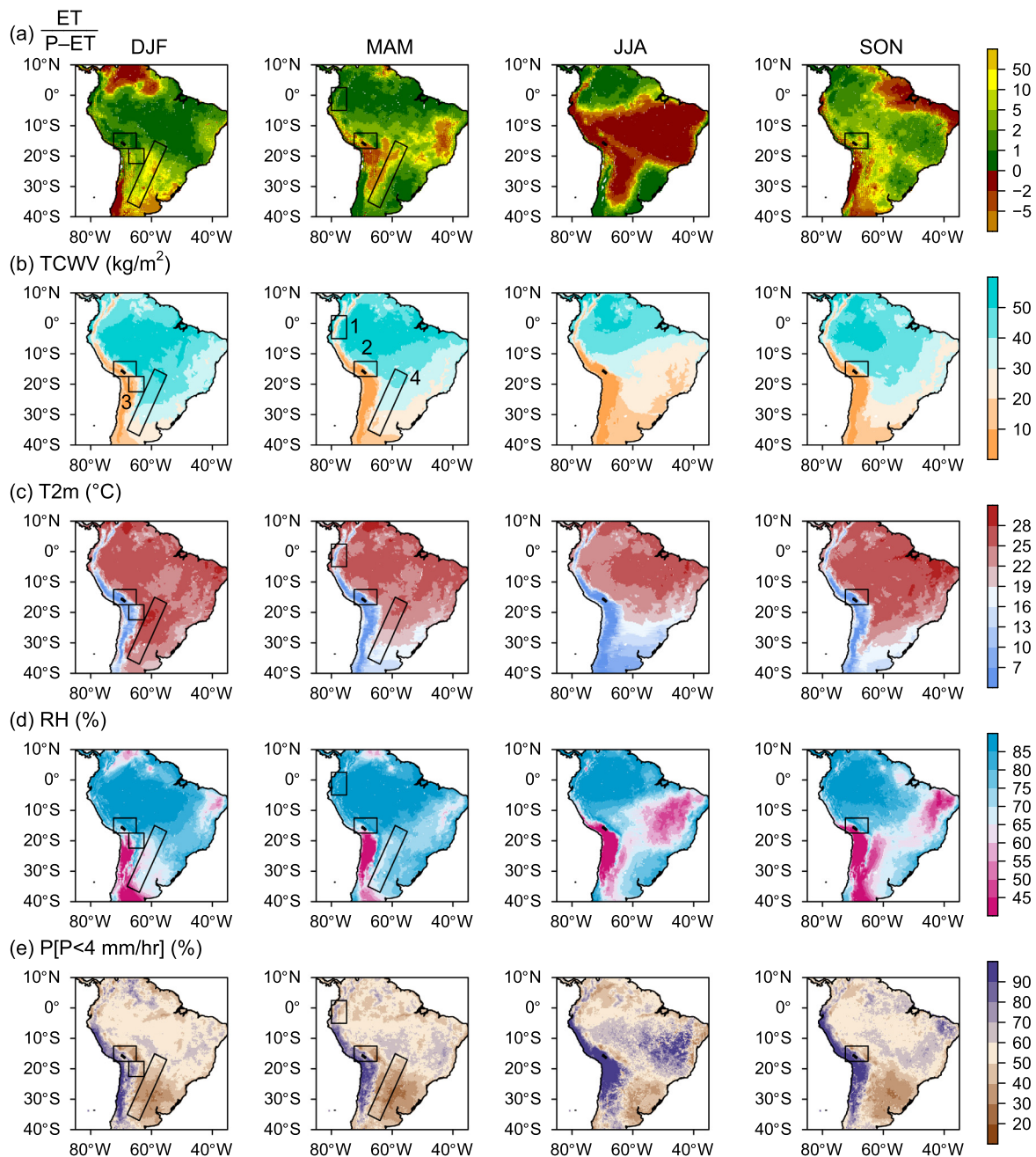


Fig. 7. The spatial pattern of model parameters over South America for different seasons. (a) Damköhler number (N_d). (b) ERA5 total column water vapor (TCWV). (c) ERA5 2-m air temperature (T2m). (d) RH calculated from ERA 2-m air and dew temperatures. (e) The percentage of rainfall that falls with rainfall rates less than 4 mm/hr, $P[P < 4 \text{ mm/hr}]$, calculated from the TRMM rainfall data. The rectangles shown in different season columns show the areas where model-data comparisons are conducted, including the (1) northern (N) Andes, (2) northern central (NC) Andes, (3) southern central (SC) Andes, and (4) South American low-level jet (LLJ) zone.

plitude and slope is enclosed between these two endmembers and eddy diffusion is likely more important in mid-latitudes (Winnick et al., 2014). For the second domain, model results are shown in its inset plot and do reproduce the shift towards lower d-excess and higher $\delta^{18}\text{O}$ for eddy-only transport but not the amplitude of d-excess shift, which is around 5‰ in model compared to 10‰ in data.

We tentatively suggest that the inability to capture that full magnitude of d-excess decrease is due to uncertainties in our derivation of initial raindrop diameter that relies on TRMM data and the Best (1950) raindrop size model. We additionally compute the percentage of rainfall that falls with rainfall rates less than 4 mm/hr from the TRMM data to represent the local rainfall intensity (Fig. 7e) and find that it decreases for the second half

of the LLJ transect (Fig. 9c). From the observed changing rainfall intensity, perhaps a combination of lighter rains and decreasing RH together result in the dramatic decrease of d-excess across the second model domain. However, we predicted an increasing initial raindrop diameter despite a decreasing final raindrop diameter and a decreasing rainfall intensity due to that a larger re-evaporative loss of raindrops has occurred under decreasing RH (Fig. S5). If we enforce the initial raindrop diameter to decrease from 1.5 mm to 1.2 mm, we find that new model results capture the full magnitude of d-excess decrease (Fig. 9a). This finding suggests that for model-data comparisons, there is a need for a more sophisticated approach to derive the initial raindrop diameter, which is an important factor to determine the isotopic effects of re-evaporation (Fig. 3). On the other hand, observations indicate that rainfall in-

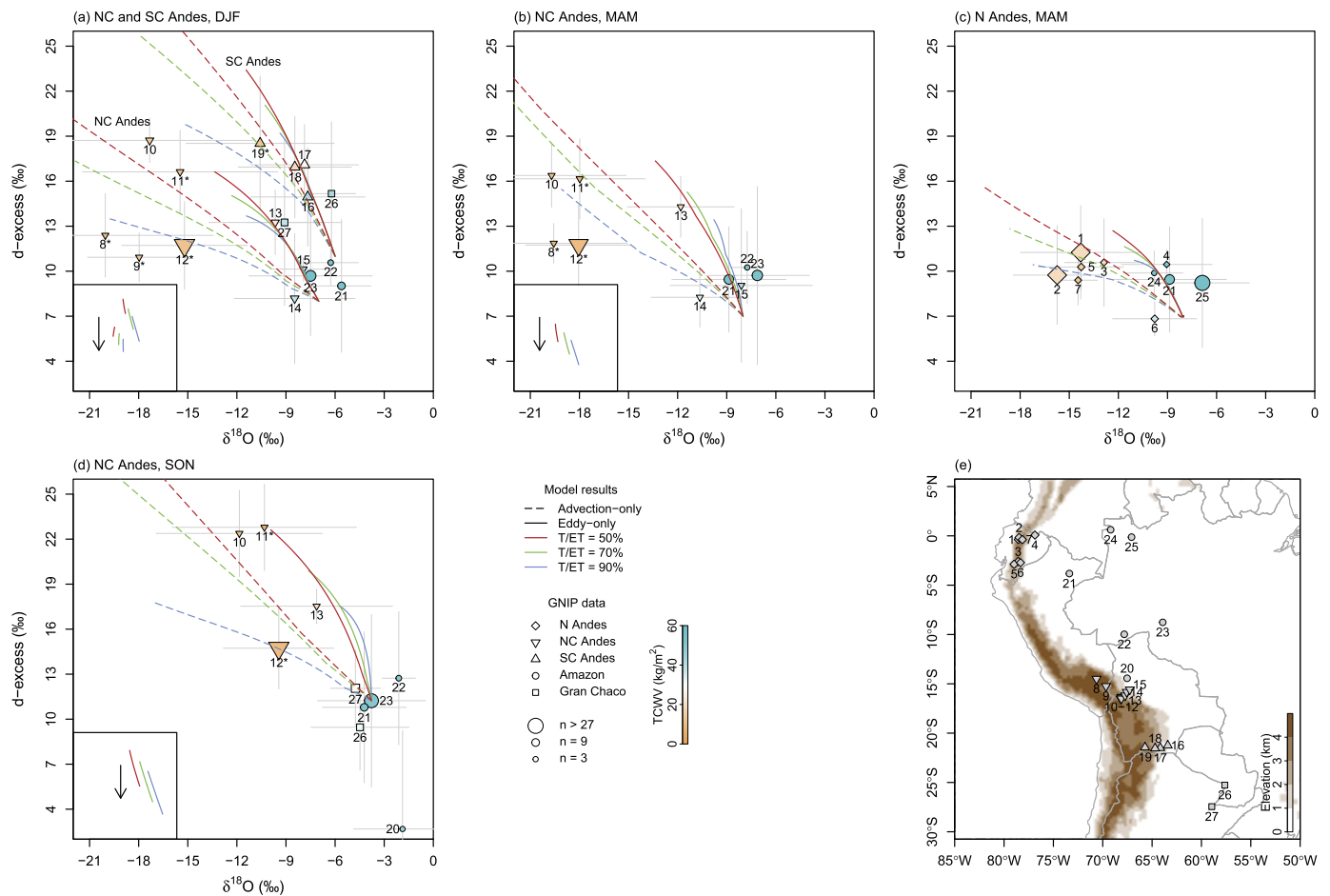


Fig. 8. The model-data comparison of the coupled changes in precipitation $\delta^{18}\text{O}$ and d-excess from the selectively analyzed Andean altitudinal transects (a–d). GNIP data points are colored to indicate the TCWV for each station and the data point size indicates the number of measurements. Error bars represent the standard deviation of monthly $\delta^{18}\text{O}$ or d-excess measurement for the respective season. Data points are labeled by unique IDs listed in the Supplementary Materials. The ID numbers with asterisks denote the stations within the plateau or intra-montane section. The model is forced by reanalysis-based parameters and run for both advection-only and eddy-only transports, with three prescribed T/ET values. The model curves shown in main plots represent the upslope section with decreasing temperature. The eddy-only model curves of plateau or intra-montane section with decreasing RH (Fig. S5) are separately shown in inset plots. These inset plots have the same axis range as their respective main plots but have a reduced plot size. (e) The map showing the locations of GNIP stations and their elevations.

tensity varies largely across climate gradients (Canel and Katz, 2018), while its role in modulating the spatial d-excess gradients is not discussed in the previous idealized model experiments.

By contrast, there is a larger temperature gradient (10°C) and a smaller RH gradient (15%) across the LLJ transect during MAM (Figs. 7c and d, and 9f). Model results reproduce the trend of GNIP data with increasing d-excess across the entire transect (Figs. 9d and e) and suggest that the raindrop re-evaporation effect would not outcompete the ET effect if the water vapor gradient is mainly driven by decreasing temperature. The outlier station 38, which is located close to the Andes (Fig. 9e), may reflect the low local rainfall intensity as shown by TRMM data (Fig. 7e).

Although the model captures different patterns of coupled $\delta^{18}\text{O}$ and d-excess changes, the slopes of model curves for the increasing d-excess during both seasons are not as steep as the actual trends of data that appear nearly vertical (Figs. 9a and d). We suggest two possible causes for why the model underestimates the relative increase of d-excess. First, RH is normalized to the 2-m temperature, but the actual RH for soil environments may be lower if normalized to the warmer skin temperature (Aemisegger et al., 2014). Second, we assume the aerodynamic exponent $q = 0.8$ for the kinetic fractionation factor of evaporation, but q may be higher for dry soils (Mathieu and Bariac, 1996). Regardless, model results

indicate again that model curves of 50% or 70% T/ET have a better fit with data than that of 90% T/ET (Figs. 9a and d).

6. Implications

The vapor transport model presented offers a unified and mechanistic understanding of how ET recycling and raindrop re-evaporation compete to drive the spatial pattern and co-variation of precipitation $\delta^{18}\text{O}$ and d-excess across terrestrial environments. Stable isotopes have been used to quantify ecohydrological processes, such as to distinguish the component of ET flux based on mass balance calculations at the large catchment or global scale (Jasechko et al., 2013; Good et al., 2015) and field measurements of stable isotopes in water vapor and xylem/soil water (Moreira et al., 1997; Williams et al., 2004), while our model exploits the spatial isotopic gradients in precipitation (Gat and Matsui, 1991). Our preliminary model-data comparison, albeit only considering two transport endmembers and lacking in statistical assessments, suggests that the T/ET is likely close to 50–70% for studied transects. This moderate percentage of regional transpiration component coincides with the estimate of other recent studies with different approaches and in different scales (Aemisegger et al., 2014; Good et al., 2015; Wei et al., 2017). Future studies can solve the vapor transport equation numerically with constrained Péclet number to

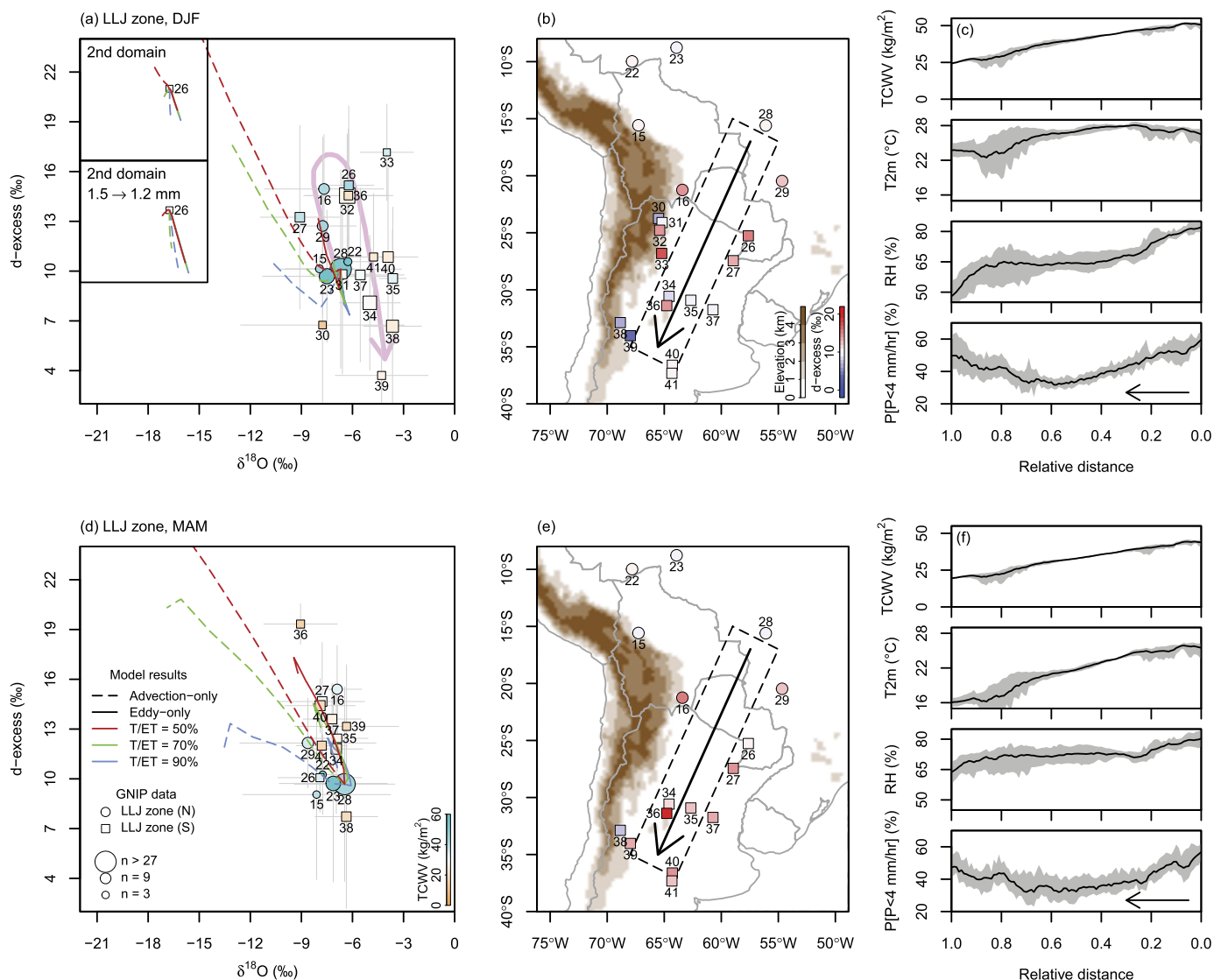


Fig. 9. The model-data comparison of the coupled changes in precipitation $\delta^{18}\text{O}$ and d-excess across the LLJ transect during (a–c) DJF and (d–f) MAM, similar to Fig. 8. The DJF main plot (a) shows the model results for the first domain in which RH does not introduce the strong local raindrop re-evaporation effect. The inset plot shows the model curves from the re-set model runs for the second domain in which RH decreases and causes the downward shift of d-excess based on the TRMM-based initial raindrop diameter or the enforced decrease of initial raindrop diameter from 1.5 to 1.2 mm. Note that the eddy-only model curves overlay each other in both main and inset plots. The pink arrow traces the “loop pattern” in data. The MAM main plot (d) shows the model results for the entire LLJ transect, in which RH does not cause any pronounced shift in the local raindrop re-evaporation effect. (b) and (e) show the locations of GNIP stations as well as their d-excess values. (c) and (f) further show the changes in relevant reanalysis-based parameters, TCWV, T2m, RH, and $P[P < 4 \text{ mm/hr}]$ across the LLJ transect, including the mean and range of values.

quantitatively link ET partitioning with isotopic gradients and variations (Kukla et al., 2019).

Our model framework offers new insights and opportunities in the use of stable isotopes for paleoaltimetry and paleoclimate reconstructions. The inverse relationship between meteoric water $\delta^{18}\text{O}$ (or $\delta^2\text{H}$) and surface elevation has been widely documented over different orogens (Gonfiantini et al., 2001; Poage and Chamberlain, 2001). This isotopic “altitude effect” has been successfully modeled as a product of the adiabatic ascent of air parcels with a Rayleigh-type rainout, and the uncertainty in the modeled relationship between $\delta^{18}\text{O}$ and elevation only arises from the surface climate condition that initiates the ascent (Rowley et al., 2001). However, Gonfiantini et al. (2001) showed that the same adiabatic ascent model could predict the observed relationship between d-excess and elevation only by fitting the proper surface climate condition and lapse rate. From our model-data comparison for the Andean altitudinal transects, we suggest that the vapor transport framework captures the physical mechanisms of both $\delta^{18}\text{O}$ and d-

excess variations across altitudinal gradients. It underscores the role of ET recycling and raindrop re-evaporation and thus may provide an alternative perspective on the highly variable correlation between $\delta^{18}\text{O}$ and elevation that the classic Rayleigh distillation process does a poor job to explain (Shen and Poulsen, 2019). Importantly, incorporating ET processes to model isotopic variations driven by orographic rainout is in line with the concept that moisture recycling is intensified over mountainous regions with both shorter length and time scales of recycling (van der Ent and Savenije, 2011). Still, we caution that the local d-excess of precipitation at high elevations could be influenced by other processes such as the contribution of water vapor from upper troposphere by vertical mixing (Samuels-Crow et al., 2014) and the transition into ice-vapor fractionation that includes a variable kinetic effect depending on the supersaturation condition (Jouzel and Merlivat, 1984).

The dependence of d-excess on ecohydrological processes and transport types described in the model also indicates that d-excess

has the potential to document past changes in the terrestrial hydrological cycle. Unfortunately, accurately measuring d-excess in paleo-meteoric water is only possible from few archives such as groundwater, fluid inclusions in speleothems, and ice cores. That said, the excess term of the triple oxygen isotope composition, $\Delta^{17}\text{O}$, can be modeled similarly to d-excess in our framework, and more importantly, may be accurately measured in proxy archives such as pedogenic carbonates (Aron et al., 2021). Overall, the same framework can be used to investigate mechanisms of hydrological and atmospheric changes in deep time that may not be constrained by $\delta^{18}\text{O}$ measurements alone, such as the effects of Neogene grassland expansion (Mix et al., 2013), the re-evaporation of plateau precipitation due to uplift (Shen and Poulson, 2019), and the strength of mid-latitude eddies under greenhouse conditions (Winnick et al., 2015).

7. Conclusions

We present a mechanistic and parsimonious model of water vapor transport to investigate the competing effects of terrestrial ET and raindrop re-evaporation on the spatial variations and gradients of precipitation $\delta^{18}\text{O}$ and d-excess. Idealized model experiments suggest that the relationship between d-excess and $\delta^{18}\text{O}$ is primarily regulated by the balance of temperature and RH controls on rainout over terrestrial environments and is further modified by the variability in ET flux and partitioning along with the atmospheric transport mechanism. This model successfully captures broad spatial variations in precipitation isotopes observed along South American transects selected to highlight the contrasting pattern in temperature- and RH-controlled rainouts. Not only this study provides the proof-of-concept in using spatial isotope data to quantify the ecohydrological processes over modern terrestrial environments, but also the framework can be applied to the triple oxygen isotope systematics for exploring the evolution of topography and hydroclimate in the geological past.

CRediT authorship contribution statement

MJW conceived the idea. ZX designed the study. ZX and MJW developed the model. ZX analyzed the model and data. ZX wrote the manuscript. MJW edited the manuscript.

Declaration of competing interest

The authors declare that they have no known competing financial interests or personal relationships that could have appeared to influence the work reported in this paper.

Code availability

The model codes are available on <https://github.com/zhx215>.

Acknowledgement

We thank Tyler Kukla, Page Chamberlain, and Annie Ritch for useful discussions related to this work, and two reviewers for comments that improved this manuscript. This work was supported by the UMass Faculty Startup Fund to MJW.

Appendix A. Supplementary material

Supplementary material related to this article can be found online at <https://doi.org/10.1016/j.epsl.2021.117120>.

References

- Aemisegger, F., Pfahl, S., Sodemann, H., Lehner, I., Seneviratne, S.I., Wernli, H., 2014. Deuterium excess as a proxy for continental moisture recycling and plant transpiration. *Atmos. Chem. Phys.* 14, 4029–4054. <https://doi.org/10.5194/acp-14-4029-2014>.
- Aron, P.G., Levin, N.E., Beverly, E.J., Huth, T.E., Passey, B.H., Pelletier, E.M., Poulson, C.J., Winkelstern, I.Z., Yarian, D.A., 2021. Triple oxygen isotopes in the water cycle. *Chem. Geol.* 565, 120026. <https://doi.org/10.1016/j.chemgeo.2020.120026>.
- Beck, H.E., Wood, E.F., Pan, M., Fisher, C.K., Miralles, D.G., van Dijk, A.I.J.M., McVicar, T.R., Adler, R.F., 2019. MSWEP V2 global 3-hourly 0.1° precipitation: methodology and quantitative assessment. *Bull. Am. Meteorol. Soc.* 100, 473–500. <https://doi.org/10.1175/bams-d-17-0138.1>.
- Best, A.C., 1950. The size distribution of raindrops. *Q. J. R. Meteorol. Soc.* 76, 16–36. <https://doi.org/10.1002/qj.49707632704>.
- Canel, L.M., Katz, J.I., 2018. Trends in U.S. hourly precipitation variance 1949–2009. *J. Hydrometeorol.* 19, 599–608. <https://doi.org/10.1175/JHM-D-17-0097.1>.
- Caves, J.K., Winnick, M.J., Graham, S.A., Sjostrom, D.J., Mulch, A., Chamberlain, C.P., 2015. Role of the westerlies in Central Asia climate over the Cenozoic. *Earth Planet. Sci. Lett.* 428, 33–43. <https://doi.org/10.1016/j.epsl.2015.07.023>.
- Craig, H., Gordon, L.L., 1965. Deuterium and oxygen 18 variations in the ocean and the marine atmosphere. In: Tongiorgi, E. (Ed.), *Stable Isotopes in Oceanographic Studies and Paleotemperatures*. Consiglio Nazionale delle Ricerche Laboratorio di Geologia Nucleare. Spoleto, pp. 9–130.
- Dansgaard, W., 1964. Stable isotopes in precipitation. *Tellus* 16, 436–468. <https://doi.org/10.3402/tellusa.v16i4.8993>.
- Fiorella, R.P., Poulson, C.J., Pillco Zolá, R.S., Barnes, J.B., Tabor, C.R., Ehlers, T.A., 2015. Spatiotemporal variability of modern precipitation $\delta^{18}\text{O}$ in the central Andes and implications for paleoclimate and paleoaltimetry estimates. *J. Geophys. Res., Atmos.* 120, 4630–4656. <https://doi.org/10.1002/2014JD022893>.
- Froehlich, K., Kralich, M., Papesch, W., Rank, D., Scheifinger, H., Stichler, W., 2008. Deuterium excess in precipitation of Alpine regions – moisture recycling. *Isot. Environ. Health Stud.* 44, 61–70. <https://doi.org/10.1080/10256010801887208>.
- Gat, J.R., Matsui, E., 1991. Atmospheric water balance in the Amazon basin: an isotopic evapotranspiration model. *J. Geophys. Res.* 96, 13179–13188. <https://doi.org/10.1029/91JD00054>.
- Gat, J.R., Bowser, C.J., Kendall, C., 1994. The contribution of evaporation from the Great Lakes to the continental atmosphere: estimate based on stable isotope data. *Geophys. Res. Lett.* 21, 557–560. <https://doi.org/10.1029/94GL00069>.
- Gimeno, L., Drumond, A., Nieto, R., Trigo, R.M., Stohl, A., 2010. On the origin of continental precipitation. *Geophys. Res. Lett.* 37, L13804. <https://doi.org/10.1029/2010GL043712>.
- Gonfiantini, R., Roche, M.-A., Olivry, J.-C., Fontes, J.-C., Zuppi, G.M., 2001. The altitude effect on the isotopic composition of tropical rains. *Chem. Geol.* 181, 147–167. [https://doi.org/10.1016/S0009-2541\(01\)00279-0](https://doi.org/10.1016/S0009-2541(01)00279-0).
- Good, S.P., Noone, D., Bowen, G., 2015. Hydrologic connectivity constrains partitioning of global terrestrial water fluxes. *Science* 349, 175–177. <https://doi.org/10.1126/science.aaa5931>.
- Graf, P., Wernli, H., Pfahl, S., Sodemann, H., 2019. A new interpretative framework for below-cloud effects on stable water isotopes in vapour and rain. *Atmos. Chem. Phys.* 19, 747–765. <https://doi.org/10.5194/acp-19-747-2019>.
- Guan, K., Pan, M., Li, H., Wolf, A., Wu, J., Medvigy, D., Caylor, K.K., Sheffield, J., Wood, E.F., Malhi, Y., Liang, M., Kimball, J.S., Saleska, Scott R., Berry, J., Joiner, J., Lyapustin, A.L., 2015. Photosynthetic seasonality of global tropical forests constrained by hydroclimate. *Nat. Geosci.* 8, 284–289. <https://doi.org/10.1038/ngeo2382>.
- Hendricks, M.B., DePaolo, D.J., Cohen, R.C., 2000. Space and time variation of $\delta^{18}\text{O}$ and δD in precipitation: can paleotemperature be estimated from ice cores? *Glob. Biogeochem. Cycles* 14, 851–861. <https://doi.org/10.1029/1999GB001198>.
- Huffman, G.J., Bolvin, D.T., Nelkin, E.J., Wolff, D.B., Adler, R.F., Gu, G., Hong, Y., Bowman, K.P., Stocker, E.F., 2007. The TRMM Multisatellite Precipitation Analysis (TMPA): quasi-global, multiyear, combined-sensor precipitation estimates at fine scales. *J. Hydrometeorol.* 8, 38–55. <https://doi.org/10.1175/JHM560.1>.
- IAEA/WMO, 2020. Global network of isotopes in precipitation. The GNIP database. Accessible at <http://www.iaea.org/water>.
- Jasechko, S., Sharp, Z.D., Gibson, J.J., Birks, S.J., Yi, Y., Fawcett, P.J., 2013. Terrestrial water fluxes dominated by transpiration. *Nature* 496, 347–350. <https://doi.org/10.1038/nature11983>.
- Jouzel, J., Merlivat, L., 1984. Deuterium and oxygen 18 in precipitation: modeling of the isotopic effects during snow formation. *J. Geophys. Res.* 89, 11749–11757. <https://doi.org/10.1029/JD089iD07p11749>.
- Kukla, T., Winnick, M.J., Maher, K., Ibarra, D.E., Chamberlain, C.P., 2019. The sensitivity of terrestrial $\delta^{18}\text{O}$ gradients to hydroclimate evolution. *J. Geophys. Res., Atmos.* 124, 563–582. <https://doi.org/10.1029/2018JD029571>.
- Lee, J.-E., Fung, I., 2008. “Amount effect” of water isotopes and quantitative analysis of post-condensation processes. *Hydrol. Process.* 22, 1–8. <https://doi.org/10.1002/hyp.6637>.
- Lee, X., Kim, K., Smith, R., 2007. Temporal variations of the $^{18}\text{O}/^{16}\text{O}$ signal of the whole-canopy transpiration in a temperate forest. *Glob. Biogeochem. Cycles* 21, GB3013. <https://doi.org/10.1029/2006GB002871>.

- Li, L., Garzzone, C.N., 2017. Spatial distribution and controlling factors of stable isotopes in meteoric waters on the Tibetan Plateau: implications for paleoelevation reconstruction. *Earth Planet. Sci. Lett.* 460, 302–314. <https://doi.org/10.1016/j.epsl.2016.11.046>.
- Liebminger, A., Haberhauer, G., Papesch, W., Heiss, G., 2006. Correlation of the isotopic composition in precipitation with local conditions in Alpine regions. *J. Geophys. Res.* 111, D05104. <https://doi.org/10.1029/2005JD006258>.
- Majoube, M., 1971. Fractionnement en oxygène 18 et deutérium entre l'eau et sa vapeur. *J. Chim. Phys.* 68, 1423–1436. <https://doi.org/10.1051/jcp/1971681423>.
- Martens, B., Miralles, D.G., Lievens, H., van der Schalie, R., de Jeu, R.A.M., Fernández-Prieto, D., Beck, H.E., Dorigo, W.A., Verhoest, N.E.C., 2017. GLEAM v3: satellite-based land evaporation and root-zone soil moisture. *Geosci. Model Dev.* 10, 1903–1925. <https://doi.org/10.5194/gmd-10-1903-2017>.
- Mathieu, R., Bariac, T., 1996. A numerical model for the simulation of stable isotope profiles in drying soils. *J. Geophys. Res.* 101, 12685–12696. <https://doi.org/10.1029/96JD00223>.
- McGuffie, K., Henderson-Sellers, A., 2004. Stable water isotope characterization of human and natural impacts on land-atmosphere exchanges in the Amazon Basin. *J. Geophys. Res.* 109, D17104. <https://doi.org/10.1029/2003JD004388>.
- Merlivat, L., Jouzel, J., 1979. Global climatic interpretation of the deuterium-oxygen 18 relationship for precipitation. *J. Geophys. Res.* 84, 5029–5033. <https://doi.org/10.1029/JC084iC08p05029>.
- Mix, H.T., Winnick, M.J., Mulch, A., Page Chamberlain, C., 2013. Grassland expansion as an instrument of hydrologic change in Neogene western North America. *Earth Planet. Sci. Lett.* 377–378, 73–83. <https://doi.org/10.1016/j.epsl.2013.07.032>.
- Moreira, M.Z., Sternberg, L.S.L., Martinelli, L.A., Victoria, R.L., Barbosa, E.M., Bonates, L.C., Nepstad, D.C., 1997. Contribution of transpiration to forest ambient vapour based on isotopic measurements. *Glob. Change Biol.* 3, 439–450. <https://doi.org/10.1046/j.1365-2486.1997.00082.x>.
- Noone, D., 2012. Pairing measurements of the water vapor isotope ratio with humidity to deduce atmospheric moistening and dehydration in the tropical midtroposphere. *J. Climate* 25, 4476–4494. <https://doi.org/10.1175/JCLI-D-11-00582.1>.
- Pang, Z., Kong, Y., Froehlich, K., Huang, T., Yuan, L., Li, Z., Wang, F., 2011. Processes affecting isotopes in precipitation of an arid region. *Tellus B* 63, 352–359. <https://doi.org/10.1111/j.1600-0889.2011.00532.x>.
- Pfahli, S., Sodemann, H., 2014. What controls deuterium excess in global precipitation? *Clim. Past* 10, 771–781. <https://doi.org/10.5194/cp-10-771-2014>.
- Poage, M.A., Chamberlain, C.P., 2001. Empirical relationships between elevation and the stable isotope composition of precipitation and surface waters: considerations for studies of paleoelevation change. *Am. J. Sci.* 301, 1–15. <https://doi.org/10.2475/ajs.301.1.1>.
- Putman, A.L., Fiorella, R.P., Bowen, G.J., Cai, Z., 2019. A global perspective on Local Meteoric Water Lines: meta-analytic insight into fundamental controls and practical constraints. *Water Resour. Res.* 55, 6896–6910. <https://doi.org/10.1029/2019WR025181>.
- Risi, C., Bony, S., Vimeux, F., 2008. Influence of convective processes on the isotopic composition ($\delta^{18}\text{O}$ and δD) of precipitation and water vapor in the tropics: 2. Physical interpretation of the amount effect. *J. Geophys. Res.* 113, D19306. <https://doi.org/10.1029/2008JD009943>.
- Risi, C., Ogée, J., Bony, S., Bariac, T., Raz-Yaseef, N., Wingate, L., Welker, J., Knohl, A., Kurz-Besson, C., Leclerc, M., Zhang, G., Buchmann, N., Santrucek, J., Hronkova, M., David, T., Peylin, P., Guglielmo, F., 2016. The water isotopic version of the land-surface model ORCHIDEE: implementation, evaluation, sensitivity to hydrological parameters. *Hydrol. Curr. Res.* 7, 258. <https://doi.org/10.4172/2157-7587.1000258>.
- Rohrmann, A., Strecker, M.R., Bookhagen, B., Mulch, A., Sachse, D., Pingel, H., Alonso, R.N., Schildgen, T.F., Montero, C., 2014. Can stable isotopes ride out the storms? The role of convection for water isotopes in models, records, and paleoaltimetry studies in the central Andes. *Earth Planet. Sci. Lett.* 407, 187–195. <https://doi.org/10.1016/j.epsl.2014.09.021>.
- Romps, D.M., 2017. Exact expression for the lifting condensation level. *J. Atmos. Sci.* 74, 3891–3900. <https://doi.org/10.1175/JAS-D-17-0102.1>.
- Rowley, D.B., Pierrehumbert, R.T., Currie, B.S., 2001. A new approach to stable isotope-based paleoaltimetry: implications for paleoaltimetry and paleohypsometry of the High Himalaya since the Late Miocene. *Earth Planet. Sci. Lett.* 188, 253–268. [https://doi.org/10.1016/S0012-821X\(01\)00324-7](https://doi.org/10.1016/S0012-821X(01)00324-7).
- Salati, E., Dall'Olio, A., Matsui, E., Gat, J.R., 1979. Recycling of water in the Amazon Basin: an isotopic study. *Water Resour. Res.* 15, 1250–1258. <https://doi.org/10.1029/WR015i005p01250>.
- Samuels-Crow, K.E., Galewsky, J., Sharp, Z.D., Dennis, K.J., 2014. Deuterium excess in subtropical free troposphere water vapor: continuous measurements from the Chajnantor Plateau, northern Chile. *Geophys. Res. Lett.* 41, 8652–8659. <https://doi.org/10.1002/2014GL062302>.
- Shen, H., Poulsen, C.J., 2019. Precipitation $\delta^{18}\text{O}$ on the Himalaya–Tibet orogeny and its relationship to surface elevation. *Clim. Past* 15, 169–187. <https://doi.org/10.5194/cp-15-169-2019>.
- Smith, W.L., 1966. Note on the relationship between total precipitable water and surface dew point. *J. Appl. Meteorol.* 5, 726–727. [https://doi.org/10.1175/1520-0450\(1966\)005<0726:NOTRBT>2.0.CO;2](https://doi.org/10.1175/1520-0450(1966)005<0726:NOTRBT>2.0.CO;2).
- Stein, A.F., Draxler, R.R., Rolph, G.D., Stunder, B.J.B., Cohen, M.D., Ngan, F., 2015. NOAA's HYSPLIT atmospheric transport and dispersion modeling system. *Bull. Am. Meteorol. Soc.* 96, 2059–2077. <https://doi.org/10.1175/BAMS-D-14-00110.1>.
- Stewart, M.K., 1975. Stable isotope fractionation due to evaporation and isotopic exchange of falling waterdrops: applications to atmospheric processes and evaporation of lakes. *J. Geophys. Res.* 80, 1133–1146. <https://doi.org/10.1029/JC080i009p01133>.
- van der Ent, R.J., Savenije, H.H.G., 2011. Length and time scales of atmospheric moisture recycling. *Atmos. Chem. Phys.* 11, 1853–1863. <https://doi.org/10.5194/acp-11-1853-2011>.
- van der Ent, R.J., Wang-Erlandsson, L., Keys, P.W., Savenije, H.H.G., 2014. Contrasting roles of interception and transpiration in the hydrological cycle – part 2: moisture recycling. *Earth Syst. Dyn.* 5, 471–489. <https://doi.org/10.5194/esd-5-471-2014>.
- Vimeux, F., Masson, V., Jouzel, J., Stievenard, M., Petit, J.R., 1999. Glacial–interglacial changes in ocean surface conditions in the Southern Hemisphere. *Nature* 398, 410–413. <https://doi.org/10.1038/18860>.
- Vuille, M., Bradley, R.S., Werner, M., Healy, R., Keimig, F., 2003. Modeling $\delta^{18}\text{O}$ in precipitation over the tropical Americas: 1. Interannual variability and climatic controls. *J. Geophys. Res.* 108, 4174. <https://doi.org/10.1029/2001JD002038>.
- Warner, M.S.C., 2018. Introduction to PySPLIT: a Python toolkit for NOAA ARL's HYSPLIT model. *Comput. Sci. Eng.* 20, 47–62. <https://doi.org/10.1109/MCSE.2017.3301549>.
- Wei, Z., Yoshimura, K., Wang, L., Miralles, D.G., Jasechko, S., Lee, X., 2017. Revisiting the contribution of transpiration to global terrestrial evapotranspiration. *Geophys. Res. Lett.* 44, 2792–2801. <https://doi.org/10.1002/2016GL072235>.
- Williams, D.G., Cable, W., Hultine, K., Hoedjes, J.C.B., Yezpe, E.A., Simonneaux, V., Er-Raki, S., Boulet, G., de Bruin, H.A.R., Chehbouni, A., Hartogensis, O.K., Timouk, F., 2004. Evapotranspiration components determined by stable isotope, sap flow and eddy covariance techniques. *Agric. For. Meteorol.* 125, 241–258. <https://doi.org/10.1016/j.agrformet.2004.04.008>.
- Winnick, M.J., Chamberlain, C.P., Caves, J.K., Welker, J.M., 2014. Quantifying the isotopic 'continental effect'. *Earth Planet. Sci. Lett.* 406, 123–133. <https://doi.org/10.1016/j.epsl.2014.09.005>.
- Winnick, M.J., Caves, J.K., Chamberlain, C.P., 2015. A mechanistic analysis of early Eocene latitudinal gradients of isotopes in precipitation. *Geophys. Res. Lett.* 42, 8216–8224. <https://doi.org/10.1002/2015GL064829>.
- Wong, T.E., Nusbaumer, J., Noone, D.C., 2017. Evaluation of modeled land-atmosphere exchanges with a comprehensive water isotope fractionation scheme in version 4 of the Community Land Model. *J. Adv. Model. Earth Syst.* 9, 978–1001. <https://doi.org/10.1002/2016MS000842>.